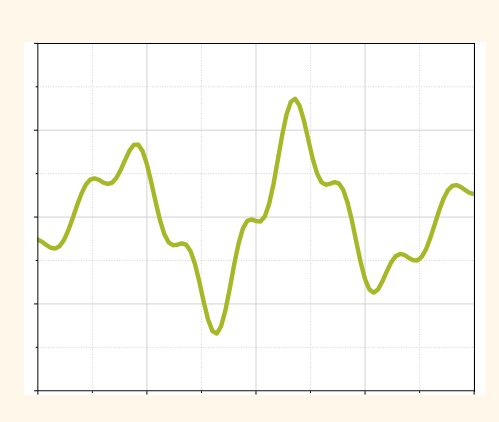
# Frequency shifts in a coherent population trapping Cs vapor cell atomic clock

Juliette Breurec, Moustafa Abdel Hafiz, Claudio E. Calosso, Oriane Lelièvre and Rodolphe Boudot

Abstract—We report on measurements of frequency shifts in a high-performance microwave cesium vapor cell atomic clock based on coherent population trapping (CPT). The dependence of the clock frequency on numerous experimental parameters, such as the laser power, the laser frequency, the microwave power, the cell temperature, the static magnetic field, but also the temperature of some key components, or the translation and rotation of critical wave plates and optical elements, is investigated. The stability budget of the clock frequency at 1 day is reported and discussed. This study constitutes a solid database for the future demonstration of a CPT-based cell clock with enhanced mid- and long-term stability performances.



Index Terms— Allan deviation, Atomic clocks, Frequency shifts, Frequency stability, Vapor cell

### I. INTRODUCTION

Microwave vapor cell atomic clocks, which rely on the interaction of a probing microwave field with optically pumped alkali atoms confined in a hot buffer gas-filled vapor cell, offer excellent fractional frequency stability in a modest size and power budget. These devices have been used in numerous scientific and technological applications such as satellite-based navigation and positioning systems [1], telecommunications, instrumentation, or metrology.

The Rb cell atomic frequency standard is the most famous vapor cell atomic clock [2]. The latter, using a lamp as an optical source, and based on the continuous optical-microwave double resonance (DR) technique, has demonstrated remarkable frequency stability results, motivating its regular deployment in GNSS constellations [3]. However, the large spectral width of the spectral lamp deteriorates the optical pumping efficiency and then the short-term stability of the clock, while light-shift effects, favored by the continuous interaction of atoms with light, degrade the long-term stability of the clock [4], [5].

- J. Breurec is with FEMTO-ST, CNRS, Université Marie et Louis Pasteur, ENSMM, 25000 Besancon, France and Thales Group, 2 rue Marcel Dassault 78140 Vélizy-Villacoublay, France. (e-mail: juliette.breurec@femto-st.fr).
- M. Abdel Hafiz, and R. Boudot, are with FEMTO-ST, CNRS, Université Marie et Louis Pasteur, ENSMM, 25000 Besancon, France. (e-mail: rodolphe.boudot@femto-st.fr).
- C. E. Calosso, is with INRIM, Strada delle Cacce, Torino, Italy. (e-mail: c. calosso@inrim.it).
- O. Lelièvre is with Thales Group, 2 rue Marcel Dassault 78140 Vélizy-Villacoublay, France (e-mail: oriane.lelievre@thalesgroup.com).

Research activities on the development of vapor cell clocks have been driven by two main perspectives. The first axis aims to achieve ultra-low power chip-scale atomic clocks (CSACs) [6]–[9]. These pocket-size references are based on coherent-population trapping (CPT) physics [10], [11] and were made possible thanks to the advent of wafer-scalable microfabricated vapor cells [12]–[20] and high-bandwidth vertical-cavity surface-emitting lasers [21]–[23]. These clocks are integrated in a volume of 15-20 cm<sup>3</sup>, consume about 125 mW and offer stabilities at the 10<sup>-11</sup> level or below at 1 hour and 1 day integration time [24]–[28]. Nevertheless, their stability performances remain insufficient to satisfy the stringent timekeeping specifications of some strategic systems.

The second axis deals with the development of vapor cell clocks with superior stability performances. These cell clocks, for which the lamp is replaced by a narrow-linewidth semiconductor diode laser, usually rely on the use of advanced pulsed Ramsey-type interrogation techniques [29] that benefit the quality factor of the detected atomic resonance while mitigating the sensitivity of its frequency to variations of the light field. In this domain, the pulsed optically-pumped (POP) Rb cell clock [30]–[33], for which optical pumping and microwave interrogation are separated in time, and detection of the clock transition is performed in the optical domain, has achieved record stability performances for a microwave cell clock, with an Allan deviation of  $1.2 \times 10^{-13}$  at 1 s, and reaching  $6 \times 10^{-16}$  at 40 000 s (with drift removal and restricted length dataset selection) [34].

An alternative to the DR approach for making microwave vapor cell clocks is to employ CPT spectroscopy. Continuous-

### **Highlights**

- Stability budget at 1 day integration time in a high-performance CPT-based Cs cell atomic clock is established and discussed.
- Measured contributions yield an estimated stability budget of 3.5 imes 10 $^{-14}$  at 1 day.
- This study will support the development of high-stability CPT-based vapor cell clocks devoted to be deployed in navigation systems, communications, instrumentation or metrology.

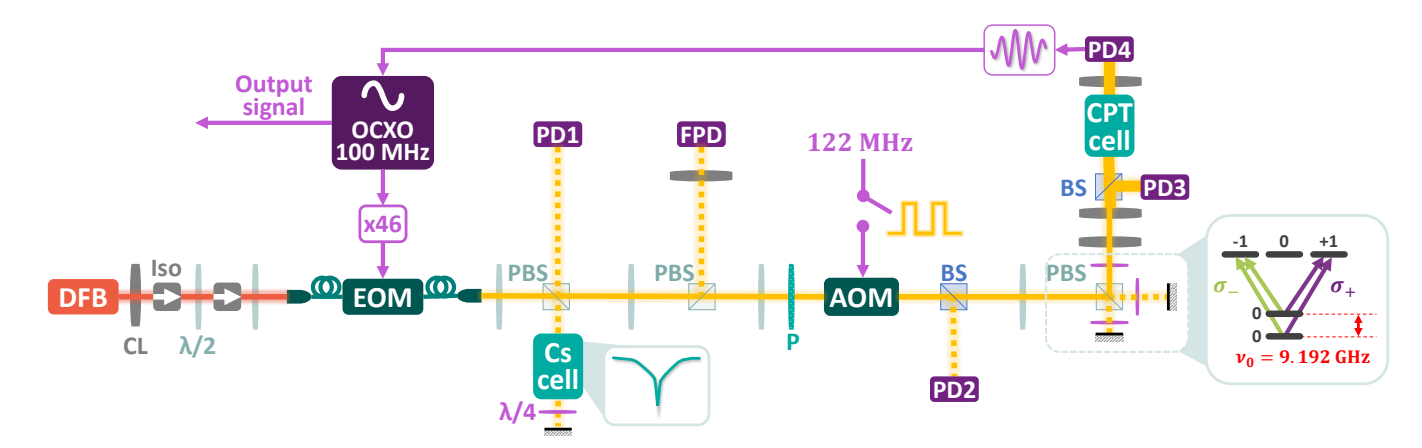


Fig. 1. Architecture of the CPT-based vapor cell atomic clock. CL: converging lens. Iso: Optical isolator.  $\lambda/2$ : half-wave plate. PBS: Polarizing beam splitter.  $\lambda/4$ : quarter-wave plate. BS: Beam splitter. FPD: Fast photodiode. PD: Photodiode. P: Polarizer.

regime CPT clocks with short-term stabilities in the low  $10^{-13}$  range at 1 s were demonstrated in [35]–[37]. Nevertheless, their stability is generally degraded after 100 s by light-shifts.

Pioneerly demonstrated by Thomas et al. [38] in a sodium atomic beam, the Raman-Ramsey clock concept [39]–[41] reveals to be an attractive approach. In recent Raman-Ramsey clocks, atoms interact with a sequence of optical CPT pulses separated by a free-evolution dark time T. Each pulse is used both for the preparation of the atoms in the dark state and for atomic signal detection. Although the frequency of CPT clocks is usually very sensitive to laser power variations [42], [43], the implementation of advanced interrogation schemes [44], such as the Symmetric Auto-Balanced Ramsey (SABR) sequence [45], [46], has demonstrated light-shift mitigation and conducted to fractional frequency stability of  $2 \times 10^{-13}$  at 1 s and, for limited-duration datasets,  $2.5 \times 10^{-15}$  at  $10^4$  s [46].

In Ref. [46], the clock instability, extracted from longer acquisitions, was limited to the level of  $3\times 10^{-14}$  at  $4\times 10^4$  s. In addition, no stability results at 1 day were reported, and only a limited number of frequency shifts were shown. In this paper, we report measurements of a significant number of frequency shifts involved in a CPT Cs cell clock, some of them never reported or studied before. The clock setup, inspired by but independent of the one described in [46], combines the optimized push-pull CPT scheme [47], [48] and SABR interrogation [46]. Coupled with fluctuations of the parameters, a stability budget of  $3.5\times 10^{-14}$  at 1 day is established.

### II. EXPERIMENTAL SETUP

Figure 1 shows the CPT clock experimental setup. The laser source is a distributed-feedback (DFB) diode laser tuned on

the Cs D<sub>1</sub> line at a wavelength of 895 nm. The laser is driven by a low-noise Libbrecht-Hall design current controller [49] with a current of 158 mA and is temperature-stabilized at about 25.5°C. A 70-dB optical isolation stage is placed at the output of the laser to prevent optical feedback. The output laser beam is injected into a fibered Mach-Zehnder electro-optic modulator (EOM). The latter is inserted into a thermal isolation box, actively temperature-controlled at 40.2°C, and driven by a low-noise microwave frequency synthesizer [50] at 4.596 GHz. Both first-order optical sidebands, frequency-split by 9.192 GHz, are used for the CPT interaction.

At the output of the EOM, the light is directed in different directions. In a first path (PD1), the light is retro-reflected into an annex glass-blown evacuated Cs vapor cell in a dualfrequency sub-Doppler spectroscopy (DFSDS) setup [51], [52], for stabilization of the laser carrier frequency. Both firstorder sidebands are, respectively, resonant with the  $F=3 \rightarrow$ F'=4 and  $F=4 \rightarrow F'=4$  Cs atom transitions. In a second path (FPD), the optical carrier power is kept minimized with a microwave synchronous detector [48]. In a third path (not shown on Fig. 1), the laser light is directed towards a Fabry-Perot interferometer to visualize the optical spectrum. In the fourth path, the light is transmitted through a voltagecontrolled linear polarizer (P) and then crosses an acoustooptic modulator (AOM). The latter, driven by a radiofrequency (RF) signal at 122 MHz, is used for shifting the laser frequency by -122 MHz (through extraction of the -1-order output diffracted beam) to compensate for the buffer gas pressure shift in the CPT cell. The AOM is also used to produce the pulsed optical Ramsey-type sequence. By turning off the RF power that drives the AOM, the light contained in the -1-order is turned off. Atoms are then in the dark. By turning on the RF power, atoms interact again with light. The total laser power can then be tuned and even stabilized by controlling the RF power that drives the AOM. The photodiode PD2 is inserted at the output of the AOM to monitor the total laser power. The AOM is inserted into a box and is actively temperature-stabilized.

The dual-frequency laser beam, after crossing a voltage-controlled half-wave plate, is sent into a Michelson-like delay-line and polarization orthogonalizer system. The latter is used to produce the push-pull optical pumping (PPOP) scheme [47], [48] that contributes to the detection of high-contrast CPT resonances. The Michelson-like system consists of two arms, each of them made of a mirror and a quarter-wave plate. A length difference of  $\lambda_{Cs}/4 \simeq 8.1$  mm (with  $\lambda_{Cs}$  the clock transition wavelength) is adjusted between the two arms. At the output of the Michelson cube, a voltage-actuated quarter-wave plate is used for obtaining the two orthogonal circularly polarized dual-frequency light fields required for PPOP.

At the output of the Michelson system, the laser beam is expanded to a diameter of about 18 mm with a telescope. The total laser power at the CPT cell input is noted  $P_L$ . A non-polarizing beam splitter cube is used to extract at the CPT cell input a fraction of the optical power, detected by the photodiode PD3. The latter, exploited for the AOM-based laser power servo, is also used for reducing the contribution of the laser amplitude-modulation (AM) noise onto the clock short-term stability. For this purpose, voltage signals  $V_4$  and  $V_3$ , respectively extracted from photodiodes PD4 (output of the CPT cell) and PD3 (input of the CPT cell), are acquired. In clock operation, the signal  $V = V_4 - kV_3$ , where k is a compensation factor that can be adjusted to mitigate the contribution of laser relative intensity noise (RIN) to the detection process [53], is used. This option, named here boost, was found to improve the clock short-term stability by a factor greater than 2 in the SABR-CPT regime.

The CPT cell is a 5-cm long and 2-cm diameter glass-blown vapor cell filled with a  $N_2$ -Ar buffer gas mixture of total pressure P=15 Torr and a mixture ratio  $r=P_{Ar}/P_{N_2}=0.56$ . The CPT cell is temperature stabilized at a set point noted  $T_{\rm cell}=34.5^{\circ}{\rm C}$  in a physics package. A static magnetic field B is applied to raise the Zeeman degeneracy. When not varied, we use B=40.9 mG. The ensemble is covered by a double-layer mu-metal magnetic shield. At the CPT cell output, the laser beam crosses a convergent lens used to focus the light on the photodiode PD4 that carries the CPT atomic signal. The optical setup of the CPT clock, currently mounted on an optical table and occupying a volume of about 40 L, is covered by a passive thermal isolation box.

The clock experiment is managed by an FPGA-based digital electronics board [54]. The latter ensures the generation of the Ramsey-type sequence and the acquisition of analog signals with ADCs. It also embeds analog outputs (DACs), among which one is used to tune the bias point of the 100 MHz oven-controlled quartz crystal oscillator (OCXO) and correct it according to the atomic resonator response. One direct digital synthesis (DDS) is used for delivering the 122 MHz signal that drives the AOM. A second DDS is used for accurate control of the amplitude, phase, and frequency of the microwave frequency synthesizer output. Once the OCXO is locked to the

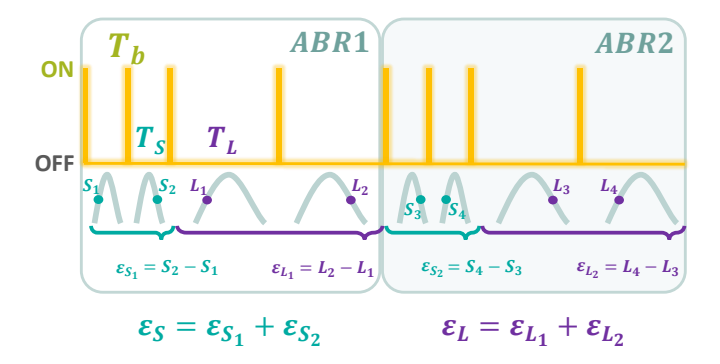
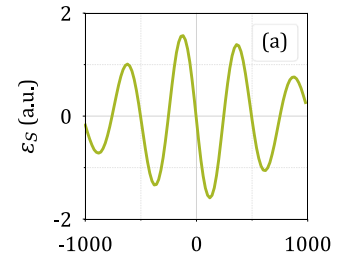
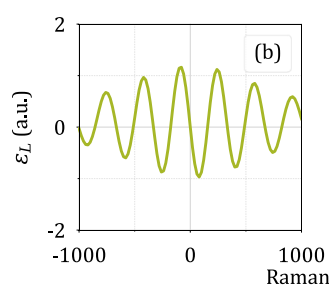


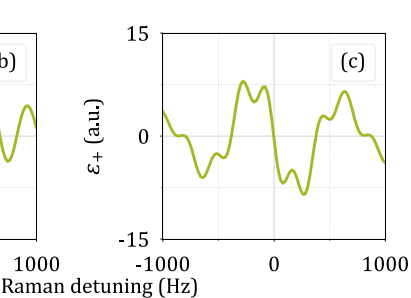
Fig. 2. Simplified representation of the SABR-CPT sequence. Sections ABR1 and ABR2 consist each on four consecutive Ramsey-CPT cycles, with two pulses separated by a short dark time  $T_S$ , followed by two pulses separated by a long dark time  $T_L$ . In the section (ABR2), the interrogation is symmetrized. Fringes are scanned in the opposite sense to the one used in section ABR1. Error signals  $\varepsilon_S$  and  $\varepsilon_L$  are ultimately generated. Corrections are applied at the end of each SABR sequence. The error signal  $\varepsilon_+ = \varepsilon_S + \varepsilon_L$  is used for correction of the local oscillator (LO) frequency while the signal  $\varepsilon_- = \varepsilon_S - \varepsilon_L$  is used for compensation of the light-shift through an additional phase increment  $\phi_c$  applied to the LO in the middle of the free evolution time of every Ramsey-CPT cycle.

atoms, its output signal at 100 MHz is compared to the signal of a reference active hydrogen maser (HM) using a signal source noise analyzer (Jackson Labs Phase station 53100A). The HM exhibits a fractional frequency stability of  $8\times 10^{-14}$  at  $1~\rm s$ ,  $5\times 10^{-15}$  at  $10^2~\rm s$ ,  $2\times 10^{-15}$  at  $10^4~\rm s$ , and then does not limit our frequency shifts measurements.

The SABR sequence used in clock operation is comparable to the one described in [46] and is illustrated in Fig. 2. It consists of two consecutive ABR sequences (ABR1 and ABR2). Each ABR sequence consists of 4 consecutive Ramsey-CPT sequences with pulses of length  $T_b = 1$  ms. In each pulse, a detection window of length  $\tau_D$  is opened after a delay noted  $\tau_d$ . The first two Ramsey-CPT patterns use a short freeevolution dark time  $T_S$  while the two following patterns use a long dark time  $T_L$ . A  $\pi/2$  phase modulation is applied to the Raman phase during dark times such that both sides of the Ramsey fringes are successively probed. Error signals noted  $\varepsilon_S$  (for pattern with dark time  $T_S$ ) and  $\varepsilon_L$  (for pattern with dark time  $T_L$ ) are generated. In the ABR2 sequence, the optical pulse sequence is the same, but the local oscillator phase modulation pattern is of opposite sign. This symmetric interrogation is important to cancel the atomic memory effect discussed in [46], [55]. Indeed, in such a vapor cell clock, the pulse repetition period is comparable or even slightly shorter than the CPT coherence lifetime, preventing the atomic state to be fully reset at each new cycle. In this situation, atoms keep a partial memory of past interactions and provide a significantly different response depending on the duration of the dark time of the preceding sequence, resulting in a bias in the light-shift estimation. The reduction of the atomic memory effect is then achieved by repeating the ABR sequence twice in a symmetric way so that two consecutive biases, of equal amplitude but opposite signs, are created and cancel each other. Ultimately, error signals  $\varepsilon_+ = \varepsilon_S + \varepsilon_L$  and  $\varepsilon_- = \varepsilon_S - \varepsilon_L$  are calculated for improved short-term stability [46]. The error signal  $\varepsilon_{+}$  is







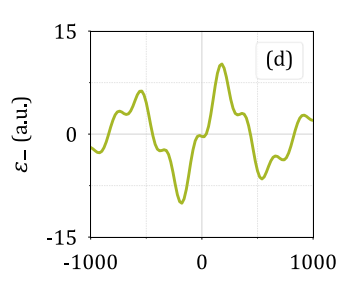


Fig. 3. Example of error signals obtained in the Ramsey-CPT (a, b) and SABR-CPT regimes (c,d), by sweeping the microwave frequency. (a): T=1.8 ms (b): T=2.8 ms.  $\varepsilon_+$  (c) and  $\varepsilon_-$  (d) are obtained here for a typical SABR-CPT sequence, with  $T_S=1$  ms and  $T_L=4$  ms. For (a) and (b), the total length of the pulses is  $T_b=955~\mu s$ . In these pulses, the detection window is opened during  $\tau_D=50~\mu s$  after a delay time  $\tau_d=5~\mu s$ . For (c) and (d), the total length of the pulses is  $T_b=1$  ms, with  $T_D=1$ 0 ms, and  $T_D=1$ 1 ms, with  $T_D=1$ 1 ms, with  $T_D=1$ 2 ms.

used for stabilization of the LO frequency while  $\varepsilon_{-}$  is used to correct the phase increment  $\varphi_c$ , added to the  $\pi/2$  Raman phase jump, to compensate for the light-shift.

In clock operation, at  $P_1 \sim 1$  mW, the SABR sequence aims to compensate for a light-shift  $\delta \nu_{ls} \sim 2.8$  Hz. With T=4ms, the phase correction  $\varphi_c$  to apply to compensate for the light-shift is then about 0.07 rad. In our setup, the 4.596 GHz output signal that drives the EOM results from the subtraction of a 204 MHz signal provided by a DDS from a 4.8 GHz signal obtained by frequency multiplication of a 100 MHz OCXO [50]. The DDS features a 14-bits DAC on its phase output. This corresponds, at 4.596 GHz, to a phase resolution  $r_{\varphi} = 2\pi/2^{14} \sim 0.4$  mrad (0.8 mrad at 9.192 GHz), yielding a resolution on the light-shift correction of about 32 mHz, i.e.  $3.5 \times 10^{-12}$  in fractional value. This resolution is not good enough to satisfy our needs. Therefore, as mentioned in [46], we apply the phase correction  $\varphi_c$  by tuning the DDS frequency, by applying frequency steps  $\Delta \nu$  of length  $\Delta t$  (with  $\Delta t = 100 \ \mu s$ ), such that  $\varphi_c = 2\pi \times \Delta \nu \times \Delta t$ . The DDS features a 48-bits DAC on its frequency output. This yields, at 4.596 GHz, a frequency resolution  $r_{\nu} = 204 \text{ MHz}/2^{48} = 0.7 \mu\text{Hz}$ (1.4  $\mu$ Hz at 9.192 GHz), i.e. a phase resolution for light-shift correction of  $8.8 \times 10^{-10}$  rad. Thus, by driving the DDS frequency (instead of the DDS phase), the resolution on the light shift correction is improved at the level of  $3.8 \times 10^{-18}$ .

## III. CLOCK SIGNAL AND SHORT-TERM STABILITY

Figure 3 plots examples of error signals,  $\varepsilon_S$  and  $\varepsilon_L$ , extracted from Ramsey sequences, obtained with  $T_S=1$  ms (a) or  $T_L=2.8$  ms (b), respectively. The best short-term stability results in the Ramsey-CPT regime were obtained with a free-evolution time T=2.8 ms.

The increase of T yields a narrowing of the Ramsey-CPT fringes, but also a reduction in signal amplitude. For  $T_L=2.8$  ms, the central Ramsey-CPT fringe, from which the error signal shown in Fig. 3(b) is extracted, exhibits a linewidth of about 178 Hz. Figure 3 also reports typical final error signals  $\varepsilon_+$  (c) and  $\varepsilon_-$  (d), obtained with the SABR-CPT sequence used in clock operation, using  $T_S=1$  ms and  $T_L=4$  ms.

Before doing dependence measurements, we have performed preliminary short-term frequency stability tests under

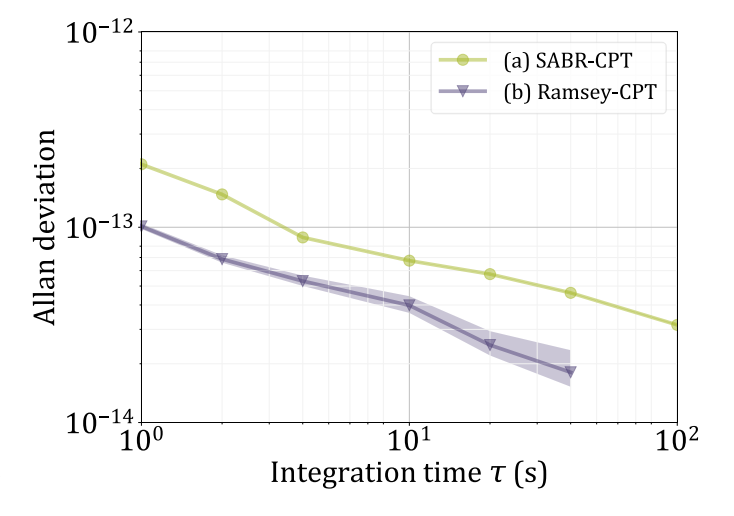


Fig. 4. Measurements of clock short-term frequency stability in various conditions. (a) SABR-CPT, with *boost*, with  $P_L$  = 1.27 mW,  $T_S$  = 1 ms and  $T_L$  = 4 ms. (b) Ramsey-CPT, with *boost*, with T = 2.8 ms and  $P_L$  = 1 mW. In all tests, other parameters of the sequence are  $T_b$  = 1 ms,  $\tau_D$  = 95  $\mu$ s and  $\tau_d$  = 5  $\mu$ s.

two conditions. The corresponding results are shown in Fig. 4. The best short-term stability performances were obtained in the Ramsey-CPT case using the *boost* option, with a free-evolution time T = 2.8 ms (b). In this case, the Allan deviation can be even slightly lower than  $1 \times 10^{-13}$  at 1 s.

In the SABR-CPT case, with the *boost* option, with  $T_S = 1$  ms and  $T_L = 4$  ms, the Allan deviation of the clock is  $2 \times 10^{-13}$  at 1 s (a). This stability is about two times worse than the one obtained in the Ramsey-CPT case.

# IV. FREQUENCY SHIFTS

In this section, we report on measurements of the dependence of the clock frequency on the variations of numerous experimental parameters. All measurements are carried out with the clock running in the SABR-CPT interrogation mode, with  $T_S=1$  ms and  $T_L=4$  ms. This dark time couple was chosen for improved light-shift mitigation, while accepting a reasonable degradation (factor of  $\sim$  2) of the clock short-term stability, in comparison with the Ramsey-CPT case (see end of section III).

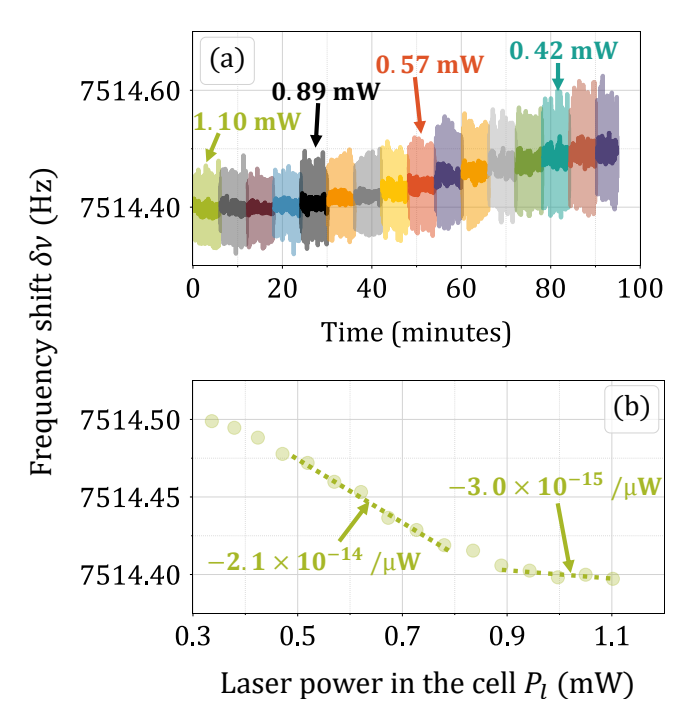


Fig. 5. (a) Temporal trace of the clock frequency shift  $\delta \nu$ . During clock operation, 16 sudden jumps of the total laser power  $P_L$  incident in the CPT cell are applied, changing the light-shift of the clock transition. Each panel shows the original data (dots) and a 50-points window moving average (solid line). Each step lasts approximately 6 minutes. (b) Clock frequency shift  $\delta \nu$  versus the total laser power  $P_L$ , extracted from (a). Dashed lines indicate a linear fit for  $P_L$  in the 0.52 - 0.78 mW range, and for  $P_L$  in the 0.89 mW - 1.1 mW range.

Among the tested parameters, some of them yield a first-order dependence of the clock frequency, while others induce a second-order dependence. Extracted dependence coefficients  $(D_p)$  can then be used, in conjunction with the measured fluctuations  $\Delta_p$  of the concerned parameter, and in the case of second-order dependences with the distance  $\Delta$  of the working point relative to the inversion point, for estimating respective contributions to the clock Allan deviation. All frequencies reported in the following graphs correspond to the offset  $\delta\nu$  from the unperturbed Cs atom frequency  $\nu_{Cs} = 9$  192 631 770 Hz, such that the measured clock frequency is  $\nu_0 = \nu_{Cs} + \delta\nu$ . We note that the main contribution to the shift  $\delta\nu$  is the collisional pressure shift ( $\sim 7.5$  kHz) induced by the presence of buffer gas in the cell. The quadratic Zeeman shift of the 0-0 clock transition, with B = 40.9 mG, is about 0.7 Hz.

### A. Light shifts

Light shifts are usually recognized as an important contribution to the mid-term stability of CPT-based vapor cell atomic clocks. Our first investigations were then focused onto the impact of the light-field parameters, including the total laser power, the laser frequency, and the microwave power. Figure 5(a) shows a time trace of the SABR-CPT clock frequency. During clock operation, sudden steps of the laser power  $P_L$  incident in the CPT cell are applied to induce a frequency shift of the clock transition frequency. For each laser power, maintained for about 5 minutes ( $\sim$  300 s), the average clock frequency is extracted. At  $\tau$  = 300 s, the clock Allan deviation

is  $3.5 \times 10^{-14}$  (see Fig. 9), ensuring the ability to detect frequency variations of 0.32 mHz, which is low enough for observing light-shifts at each power step. The total duration of the measurement shown in Fig. 5(a) is about 90 minutes ( $\sim 5400$  s). At this averaging time, the clock fractional frequency stability is below  $2 \times 10^{-13}$  (see Fig. 9), that corresponds to a frequency measurement resolution lower than 2 mHz. Again, this resolution is high enough to measure the clock frequency change ( $\sim 0.1$  Hz) between the beginning and the end of the measurement. Note that this statement applies to all the light shifts measurements presented in this paper. In this test, 16 values of the laser power were successively applied.

Derived from Fig. 5(a), Fig. 5(b) reports the clock frequency shift  $\delta \nu$  versus the laser power  $P_L$ . In this plot, a deviation of the power light-shift curve from a linear behavior is observed. Non-linear light-shift trends have already been observed in several CPT clock experiments, including coldatom CPT clocks [56]-[59] or vapor cell CPT clocks [46], [60]. In our experiment, the light-shift trend also depends on how the SABR sequence is able to resolve light-shifts and compensate for them. Fitting data in the 0.9 - 1.1 mW range by a linear function, we obtain a sensitivity coefficient of the clock frequency to laser power of  $-2.8 \times 10^{-5}$  Hz/ $\mu$ W, i.e.  $-3.0 \times 10^{-15} / \mu W$  in fractional value. This coefficient is comparable to the one reported in [46]. For comparison, a linear fit to the data around the power set point of 650  $\mu W$  yields a coefficient of  $-1.9 \times 10^{-4}$  Hz/ $\mu$ W, i.e.  $-2.1 \times 10^{-14}/\mu$ W in fractional value.

Derived from the same methodology, Fig. 6 reports the evolution of the clock frequency shift  $\delta \nu$  with multiple experimental parameters. Figure 6(a) shows the impact of microwave power  $P_{\mu W}$  measured at the EOM input port. In our setup, changes of the microwave power mainly induce variations of the total resonant power but might also cause slight changes of the optical sideband ratio, and then off-resonant lightshifts [58]. In normal clock operation conditions, we have  $P_{\mu W} \simeq 350$  mW. In the 200 - 420 mW range, we observe a roughly linear dependence from which a fractional sensitivity coefficient of  $-2.3 \times 10^{-17} / \mu W$ , i.e.  $7.9 \times 10^{-14} / \%$ , is extracted. This sensitivity is close to the one reported  $(10^{-13})$ /%) in [46]. Also, for comparison, we have measured a sensitivity of  $1.2 \times 10^{-12}$ /% in the Ramsey-CPT case (with dark time T = 2.8 ms), confirming the interest of the SABR interrogation for reducing light-shifts.

We have then investigated the influence of the laser frequency  $f_L$ . For this purpose, the separation between absorption profiles detected in the annex Cs vapor cell was used to calibrate the frequency axis and measure the voltage-frequency tuning of the laser current driver modulation input. In the region of interest, we found a linear dependence of the clock frequency on laser frequency variations of  $3.7 \times 10^{-13}$ /MHz, a value slightly higher than the one reported in [46]  $(2.4 \times 10^{-13}$ /MHz). During this measurement campaign, we have evaluated the fractional frequency stability of the DFB laser, when locked to the DFSDS setup [51]. For this purpose, a beatnote was generated between our laser and an ultra-stable optical signal at 895 nm extracted from

an optical frequency comb disciplined to a cavity-stabilized laser (see performances in [61], [62]), itself referenced to a hydrogen maser for integration times higher than 100 s. From a beatnote measurement, the instability of our DFB laser was measured at the level of  $1.5 \times 10^{-12}$ ,  $6.5 \times 10^{-13}$  and  $1 \times 10^{-11}$  at 1,  $10^2$  and  $10^4$  s respectively. The contribution of the laser frequency to the clock Allan deviation is then estimated at the level of  $1.8 \times 10^{-16}$ ,  $8 \times 10^{-17}$  and  $1.2 \times 10^{-15}$  at 1, 100 and  $10^4$  s respectively. Assuming a  $\tau$ -slope drift of the laser frequency from  $10^4$  to  $10^5$  s (worst situation), we would then have a laser stability of  $1 \times 10^{-10}$  at  $10^5$  s, contributing to the clock stability at 1 day at the level of  $1.2 \times 10^{-14}$ .

## B. Zeeman shift and buffer-gas collisional shift

Two other experimental parameters generally suspected of limiting the long-term stability of vapor cell clocks are the Zeeman shift and the buffer gas pressure collisional shift. As reported in Fig. 6(b), we have measured the dependence of the clock frequency on the static magnetic field B. We extracted from our data a quadratic dependence of about 316 Hz/ $B^2$ , i.e. 3.4 × 10<sup>-8</sup>  $B^{-2}$  (with B in Gauss). This measured value is smaller than the expected quadratic Zeeman shift of  $\sim 427 \text{ Hz/}B^2$  for the Cs atom clock transition. This discrepancy might be explained by the inhomogeneity of the B-field along the 5-cm-long cell and was not observed in a 2cm-long cell. Fluctuations of the B-field, measured by locking the synthesizer frequency onto the magnetic-field sensitive 1 -1 transition, are estimated at the level of 1  $\mu$ G at 1 day, contributing to the clock Allan deviation at  $2.7 \times 10^{-15}$  at 1 day. We have also measured the typical fluctuations of the current source that drives the B-field solenoid to estimate their impact on the clock instability. Fluctuations of the Bfield current source contribute at the level of  $4.6 \times 10^{-16}$  on the clock Allan deviation at 1 day. Figure 6(c) represents the evolution of the clock frequency in SABR-CPT mode with the temperature  $T_{\rm cell}$  of the CPT cell. The latter is measured by a thermistor placed in the copper bed that supports the cell. With the use of a N<sub>2</sub>-Ar buffer gas mixture, a quadratic dependence is observed, culminating at the inversion point  $T_{\rm inv} \simeq 34.6^{\circ} {\rm C}$ . This inversion point is in good agreement with the one predicted using collisional coefficients reported in [63]. Around this point, the dependence coefficient is in absolute value  $3.6 \times 10^{-12} \text{ K}^{-2}$ , in fractional value.

## C. EOM and AOM temperatures

We have also measured the impact of temperature variations of some key components along the optical setup on the clock frequency. Figure 6(d) shows the evolution of the clock frequency with the EOM temperature  $T_{\rm EOM}$ . A change of sign of the EOM temperature to clock frequency dependence is observed around 41°C, yielding in the 39 - 43°C range a dependence coefficient  $D_p$  of  $1.9 \times 10^{-13}~{\rm K}^{-2}$ . We checked that the clock frequency variations in this test could not be explained by EOM temperature-induced laser power variations (power stabilization active). We have performed the same exercise with the AOM temperature  $T_{\rm AOM}$ . The result is shown in

Fig. 6(e). The experimental data are well fitted by a sinusoidal dependence, highlighting the existence of specific inversion points at about 41 and 48.2°C around which the sensitivity of the clock frequency is canceled at the first order. We checked that this clock frequency dependence could not be explained by laser power variations induced by the AOM temperature change (power stabilization active). In our setup, a linear polarizer is placed at the AOM input to ensure fixed linearly polarized light, aligned with the AOM crystal axis. The latter is made of tellurium dioxide (TeO<sub>2</sub>), known to be a highly temperature-sensitive birefringent material. With temperature variations of the AOM, orthogonal components of the linearly polarized light of the ordinary and extraordinary axes of the crystal are subject to rotate at the output of the AOM [64]. We found that this temperature-induced polarization change induces the sinusoidal profile observed in Fig. 6(e). We chose to operate the AOM at 41°C. Around this point, the measured dependence coefficient is in fractional value  $1.7 \times 10^{-12}/\mathrm{K}^2$ .

# D. EOM bias voltage

Figure 6(f) reports the evolution of the clock frequency with a change in the EOM bias voltage  $V_{\rm bias}$ , when the active carrier suppression scheme is not active. In this case, changing the EOM bias voltage induces a change of the optical spectrum at the output of the EOM. We first did this test in the Ramsey-CPT regime, giving the result shown by the gray data in Fig. 6(f). Interestingly, a nice quadratic dependence, centered here on the turnover bias point of about -6.75 V, is obtained. This turnover point occurs close to the EOM bias voltage point for which the optical carrier reduction is maximized. Away from this point, the power contained in the carrier increases again and the contribution of off-resonant light-shifts is changed. We did a similar study in the SABR-CPT mode. In this case, we observe a drastic reduction in the clock frequency dependence to variations of the EOM bias voltage. In the SABR-CPT mode, the fitting of experimental data points by a linear function, close to the turnover point, yields in fractional value a dependence coefficient of  $1.2 \times 10^{-12}$ /V.

### E. Michelson system

A non-correct adjustment of the length difference d between the two arms of the Michelson system shifts the system away from the required  $\pi$  phase difference between the two dual-frequency circularly-polarized light fields. This phase mismatch can deteriorate the amplitude of the 0-0 clock transition and then the short-term stability of the clock. Due to the induced change in the atom-light interaction strength, it also causes a variation of the light shift experienced by the atoms in the vapor.

Using a voltage-controlled translation stage holding the mirror in one of the Michelson arm, we extracted, close to the clock operation point, a sensitivity of the clock frequency to length variations of the Michelson system at the level of  $8.3 \times 10^{-15}/\mu m$ .

We have then measured the typical length fluctuations of the Michelson system ensemble. For this purpose, we have used the Michelson system as an optical interferometer by

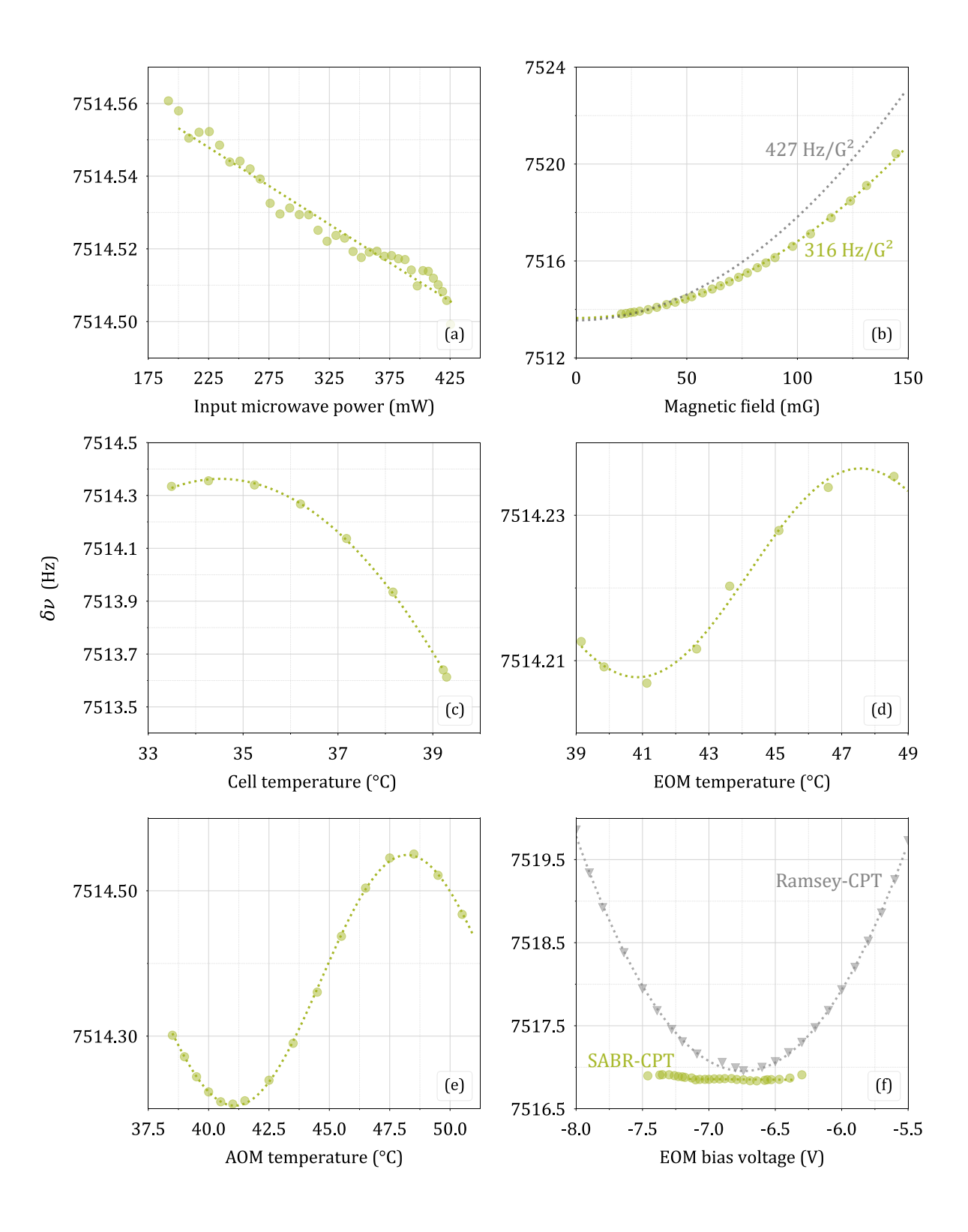


Fig. 6. Clock frequency shift  $\delta\nu$  as a function of the microwave power (a), the magnetic field (b), the CPT cell temperature (c), the EOM temperature (d), the AOM temperature (e) and the EOM bias voltage (f). Dashed lines on data of (a) and (f) (SABR-CPT case) are linear fits. Dashed lines on data of (b), (c), and (f) (Ramsey-CPT) are second-order polynomial fits. Dashed lines on data of (d) and (e) are sinusoidal fits. In subplot (f), dashed lines are quadratic (Ramsey-CPT) and linear (SABR-CPT) fits to the data.

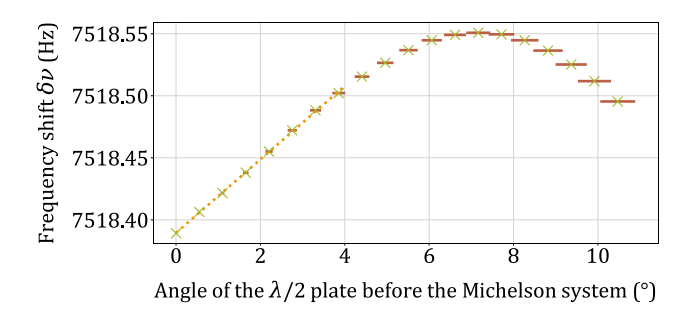


Fig. 7. Clock frequency shift  $\delta \nu$  as a function of the angular position of the half-wave plate placed before the Michelson cube. During clock operation, 20 steps are applied with a piezo motor. The zero-point corresponds to a position where the CPT clock signal is optimized. Each step lasts 3 minutes. Experimental parameters are  $T_S=1$  ms,  $T_L=4$  ms,  $P_L=645~\mu W$ . Error bars in the angle are represented by horizontal lines. In this test, the half-wave plate is mounted on a rotating support driven by a voltage-controlled piezoelectric motor. Each time the voltage is incremented, the rotation angle, as well as its uncertainty, are increased.

adding to its output a polarizer tilted at 45° from the beam orthogonal polarization axes. In this test, the microwave signal was turned off so that a single-frequency optical field was used. After proper calibration of the interferometer transfer function, voltage fluctuations at the output of the polarizer can then be converted into length fluctuations. Along a 7-days measurement, the maximum length fluctuation was measured to be lower than 22 nm, corresponding to a variation of 39  $\mu rad$  of the phase difference. The contribution of this effect on the clock Allan deviation is therefore estimated at the level of  $3\times 10^{-18}$  at 100 s and  $1.8\times 10^{-16}$  at  $10^5$  s.

# F. Translation and rotation of wave plates

We have later evaluated, in our table-top experimental setup, the impact of the rotation of polarizing plates. Figure 7 shows the clock frequency shift  $\delta\nu$  versus the angular position  $\theta_{\lambda/2}$  of the half-wave plate (HWP) before the Michelson system.

In this test, we noted as the starting angle of  $0^{\circ}$  the position of the HWP for which the signal and short-term stability were optimized, expected to be close to the condition where the components  $\sigma^+$  and  $\sigma^-$  of the PPOP scheme are well balanced. Deviating from this reference angle implies perturbing the optical power distribution equilibrium between the two arms of the Michelson system.

In our test, an inversion point about 7° away from the initial position (0° starting angle) is visible. The reason for the existence of this turning point, as well as its position, is not clearly explained to date. We suggest that the evolution of the clock frequency with rotation of the half-wave plate might result from frequency shifts of different kinds, mainly light-shifts and Rabi pulling-like effect.

Unbalanced intensities of  $\sigma^+$  and  $\sigma^-$  polarized light fields could lead to an optimized polarization scheme that maximizes the atom-field interaction, and thus light shift. In addition, the Zeeman spectrum becomes asymmetric. Through optical pumping, populations are mainly transferred to the extreme Zeeman sub-levels. Transitions neighboring to the 0-0 clock

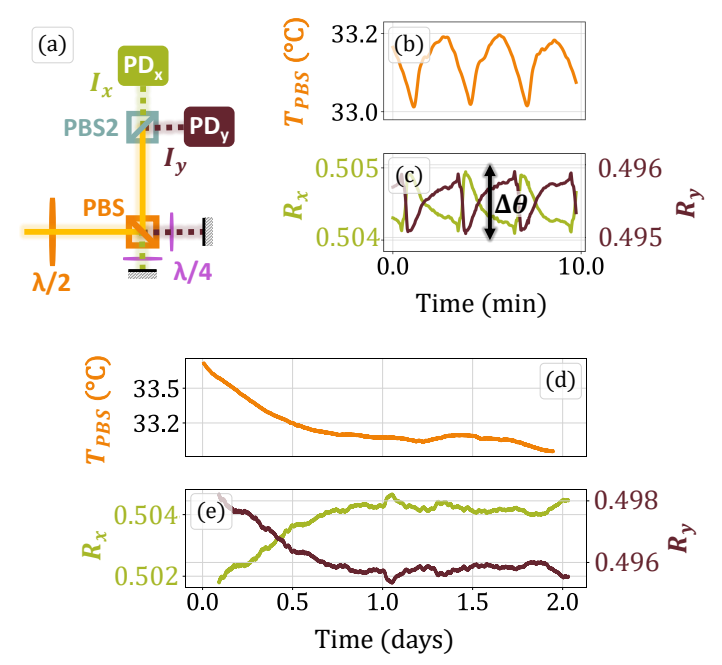


Fig. 8. (a) Scheme implemented to study the influence of temperature variations of passive optical components temperature (half-wave plate before, and PBS inside the Michelson system) on the optical power distribution. Both components are equipped with a heating resistor and temperature sensors. (b) Forced oscillations of the PBS temperature  $T_{PBS}$ , measured with a sensor placed on the cube post, observed during 10 minutes. (c) Variations of the optical power distribution between the two arms of the Michelson  $R_x$  and  $R_y$ , for PDx and PDy signals, induced by variations of  $T_{PBS}$  depicted in (b).(d) Long-term variations of  $T_{PBS}$ , measured by a sensor placed on the top surface of the cube. The temperature evolution was measured after having closed the box that surrounds the optics setup, explaining the time ( $\sim$  1 day) to reach more stable conditions. (e) Long-term variations of  $R_x$  and  $R_y$ , induced by variations of  $T_{PBS}$  shown in (d). (d) and (e) are the result of a 500-points window-moving average.

transition can then add to the 0-0-resonance signal and distort the 0-0 resonance. This phenomenon is analog to the well-known Rabi pulling effect. The amplitude of this shift depends then on the applied Zeeman splitting and on the relative amplitude and width between the 0-0 Zeeman resonance and the neighboring ones. These effects could lead to the existence of a turning point with respect to the half-wave plate angle, due to light shift effects, that might be shifted away from the angle of balanced circularly polarized light, caused by the additional Rabi-pulling-like effect.

Using a linear fit near the initial starting point (0°), away from the inversion point, we obtain a dependence coefficient of the clock frequency to the angular position of the half-wave plate  $\theta_{\lambda/2}$  of  $3.2 \times 10^{-12}$ /°, in fractional value. We conducted similar studies for the polarizer placed before the AOM and the quarter-wave plate placed at the output of the Michelson system, extracting the respective coefficients  $\theta_P = -2.1 \times 10^{-13}$ /° and  $\theta_{\lambda/4} = 1.8 \times 10^{-13}$ /°.

### G. Temperature of passive optical components

Other sensitivities we had never investigated are linked to temperature variations of some passive optical components. Here, we paid attention to the PBS and the half-wave plate of

### TABLE I

Dependence coefficient  $D_p$  of the clock frequency (in fractional value) to experimental parameters, fluctuations  $\Delta p$  of the parameter at 1 day, and contribution  $\sigma_p$  of fluctuations of those parameters to the clock stability at 1 day. For parameters with a first-order dependence coefficient,  $\sigma_p = D_p \times \Delta p$ . For parameters with a second-order dependence coefficient, we have  $\sigma_p = 2 \times D_p \times \Delta \times \Delta p$ , with  $\Delta$  the distance of the working point with respect to the inversion point.  $\Delta$  values of 0.04 G, 0.1 K, 0.05 K and 0.015 K were used for B,  $T_{\rm AOM}$ ,  $T_{\rm EOM}$  and  $T_{\rm cell}$ , respectively. Fluctuations of the laser power and of the B-field indicated in the second column are measured "in-loop". These contributions might then be under-estimated.

Parameter	Symbol	Dependence $D_p$	$\Delta p$ (1 day)	$\sigma_p$ (1 day)
PBS temperature	$T_{\mathrm{PBS}}$	$7.9 \times 10^{-13}$ /K	$4.1 \times 10^{-2} \text{ K}$	$3.2 \times 10^{-14}$
Laser frequency	$f_L$	$3.7 \times 10^{-13} \text{ /MHz}$	$3.3 \times 10^{-2} \text{ MHz}$	$1.2 \times 10^{-14}$
$\lambda/2$ temperature	$T_{\lambda/2}$	$1.7 \times 10^{-13} / \text{K}$	$4.1 \times 10^{-2} \text{ K}$	$7.0 \times 10^{-15}$
Microwave power	$P_{\mu W}$	$-2.3 \times 10^{-17} / \mu W$	170 μW	$3.9 \times 10^{-15}$
Magnetic field	$\mid B \mid$	$3.4 \times 10^{-8} / G^2$	$1.0 \mu G$	$2.7 \times 10^{-15}$
AOM temperature	$T_{AOM}$	$1.7 \times 10^{-12}  / \mathrm{K}^2$	$1.5 \times 10^{-3} \text{ K}$	$5.1 \times 10^{-16}$
B-field current	$I_B$	$5.8 \times 10^{-13}  \text{/mA}^2$	$2.4 \times 10^{-5} \text{ mA}$	$2.8 \times 10^{-16}$
Michelson length	$\mid d \mid$	$-8.3 \times 10^{-15} / \mu \text{m}$	$2.2 \times 10^{-2} \ \mu {\rm m}$	$1.8 \times 10^{-16}$
CPT cell temperature	$T_{\rm cell}$	$-3.6 \times 10^{-12} / \text{K}^2$	$1.5 \times 10^{-3} \text{ K}$	$1.6 \times 10^{-16}$
$\lambda/2$ angle	$\theta_{\lambda/2}$	$3.2 \times 10^{-12} / ^{\circ}$	$4.3 \times 10^{-5}$ °	$1.4 \times 10^{-16}$
Polarizer angle	$\theta_P$	$-2.1 \times 10^{-13} / ^{\circ}$	$4.3 \times 10^{-5}$ °	$9.0 \times 10^{-18}$
$\lambda/4$ angle	$\theta_{\lambda/4}$	$1.8 \times 10^{-13}  / ^{\circ}$	$4.3 \times 10^{-5}$ °	$7.7 \times 10^{-18}$
Laser power	$P_L$	$-3.0 \times 10^{-15} / \mu W$	$2.4 \times 10^{-3} \ \mu W$	$7.2 \times 10^{-18}$
EOM temperature	$T_{\rm EOM}$	$1.9 \times 10^{-13}  / \text{K}^{2}$	$9.6 \times 10^{-5} \text{ K}$	$1.8 \times 10^{-18}$
Total	$\sqrt{\sum \sigma_p^2}$			$3.5 \times 10^{-14}$

the Michelson system. Indeed, a temperature change of these components has a direct impact on the distribution of optical power between the two arms of the Michelson system and then on the symmetry of the Zeeman spectrum.

The sensitivity  $S_T$  of the clock frequency  $\nu_0$  to the temperature T of passive optical components is defined as:

$$S_T = \frac{d\nu_0}{dT} = \frac{d\nu_0}{d\theta} \frac{d\theta}{dT} \tag{1}$$

Here,  $\frac{d\nu_0}{d\theta}$  represents the sensitivity of the clock frequency to the rotation of the half-wave plate, measured in Section IV-F to be in fractional value  $3.2\times 10^{-12}/^{\circ}$ , or  $1.8\times 10^{-10}/\mathrm{rad}$ .  $\frac{d\theta}{dT}$  indicates the sensitivity of the angle of the major polarization axis with respect to the component temperature. To measure  $\frac{d\theta}{dT}$ , we placed a PBS (PBS2) at the output of the Michelson system, as shown in Fig. 8(a), to separate orthogonal components of the light field. These components are detected by photodiodes  $\mathrm{PD}_x$  and  $\mathrm{PD}_y$ , recording intensities  $I_x = I_0 \cos^2(\theta)$  and  $I_y = I_0 \sin^2(\theta)$ , where  $I_0 = I_x + I_y$  is the total power at the output of the device.

A resistive heater was used to induce temperature oscillations in the PBS, with a period of approximately 195 s and a peak-to-peak amplitude of 0.17 K, as depicted in Fig. 8(b). This temperature fluctuation resulted in variations in the fractional optical power in each arm by 0.075%, illustrated by the signals  $R_x = \frac{I_x}{I_0}$  and  $R_y = \frac{I_y}{I_0}$ , shown in Fig. 8(c). Angle fluctuations can be derived by considering the slope of  $R_y(\theta) = \sin^2(\theta)$  around  $\theta = \pi/4$ , which is the working point that equally splits the power between the two arms, given by  $2\sin(\theta)\cos(\theta)|_{\theta=\frac{\pi}{4}}=1\,\mathrm{rad}^{-1}$ . In this specific case, 0.075% corresponds to 7.5 mrad, yielding  $\frac{d\theta}{dT}=4.4\,\mathrm{mrad/K}$  and thus a PBS thermal sensitivity  $S_T$  of  $7.9\times10^{-13}/\mathrm{K}$ .

Following the same methodology for the half-wave plate, a sensitivity of  $1.7 \times 10^{-13}$ /K is obtained. These values highlight a relevant sensitivity of the clock frequency to temperature

variations of these passive optical components, especially for the cube. Individual stabilization of their temperature could then be needed to achieve improved clock long-term stability. For additional information, Figures 8(d) show long-term variations of the cube temperature and 8(e) those of  $R_x$  and  $R_y$ .

# H. Resume

Table I summarizes the measured dependence coefficients, noted  $D_p$ , of the clock frequency (in fractional value) on the experimental parameters, the typical fluctuations  $\Delta p$  at 1 day of these parameters (around their set-point), and the contribution of these parameters to the clock stability at 1 day. In this table, the laser frequency instability at 1 day was extrapolated from a measurement limited at 10<sup>4</sup> s integration time, assuming a  $\tau$ -slope drift of the laser frequency from  $10^4$ and  $10^5$  s. Thus, the laser frequency contribution is considered as an upper bound. In this list, major contributions to the clock instability at 1 day are temperature variations of the Michelson PBS, the laser frequency, the microwave power, temperature variations of the half-wave plate at the PPOP Michelson input and the static magnetic field. All other contributions are calculated to be below the  $10^{-15}$  level and should not limit performance to date. In Table I, the quadratic sum of all contributions leads to an estimated clock instability budget of  $3.5 \times 10^{-14}$  at 1 day. We note that this stability budget at 1 day is close to the measured clock stability (original data, without drift removal) of high-performance Rb POP clocks [34], [65].

# V. DISCUSSIONS AND ADDITIONAL INVESTIGATIONS

To date, the actual measured clock stability, shown in Fig. 9, extracted from raw data, is  $9 \times 10^{-14}$  at 1 day. This stability is higher than any contribution reported in Table I,

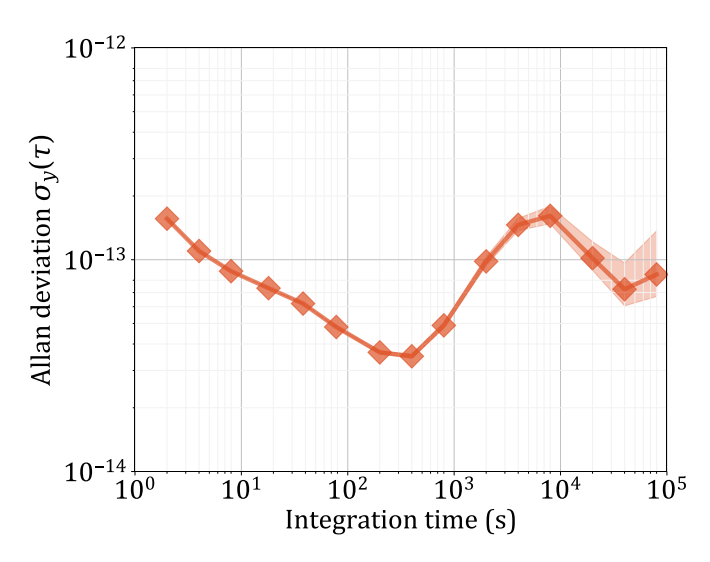


Fig. 9. Measured Allan deviation of the clock frequency. Original data are used. No drift removal was undertaken.

but also higher, by a factor of  $\sim$  2.6, than the total budget  $(3.5 \times 10^{-14})$  reported in Table I. In addition, unexplained degradation of clock stability is currently observed for integration times higher than 100 s. This analysis might indicate that the main limitation to the clock stability at 1 day has not yet been identified.

Additional investigations we conducted include a calculation of the impact of the barometric effect [65]. Using our cell dimensions and contents, the sensitivity of the clock frequency to atmospheric pressure is estimated at the level of  $2.3 \times 10^{-14}$ /hPa. Typical fluctuations of the atmospheric pressure in the laboratory were measured in the 2 - 5 Pa range at 100 s and 1 - 7.5 hPa at 1 day. This effect would then limit the stability of the clock at a level lower than  $1.2 \times 10^{-15}$  at 100 s, and then can not explain the stability degradation at 100 s. At the opposite, at 1 day, this effect might explain stability up to the level of  $1.7 \times 10^{-13}$ . This effect should then be considered with much caution for long-term stability of the clock.

Interestingly, by monitoring the laser beam profile over time before the AOM during standard clock operation, we observed a possible correlation between the clock frequency, horizontal position of the beam and the diameter of the beam. This is illustrated in Fig. 10. Specifically, the position seems related to the trend of the frequency (medium-long term), while the diameter might be responsible of the "fast" fluctuations and then of the bump appearing on the clock Allan deviation shown in Fig. 9. We suspect then that the clock frequency could be perturbed by residual light-shifts induced by inhomogeneous laser intensity distribution in the CPT vapor cell [66]. In the future, we plan to actually measure the sensitivity of the clock frequency to variations of the beam diameter or position. If confirmed that this effect is critical, stabilizing the laser intensity (not only the laser power) incident in the CPT cell to see how it impacts the clock stability might be a first option.

Some other aspects remain to be studied. For example, the contribution of the CPT cell temperature is currently estimated through the measurement of a single sensor placed at a specific

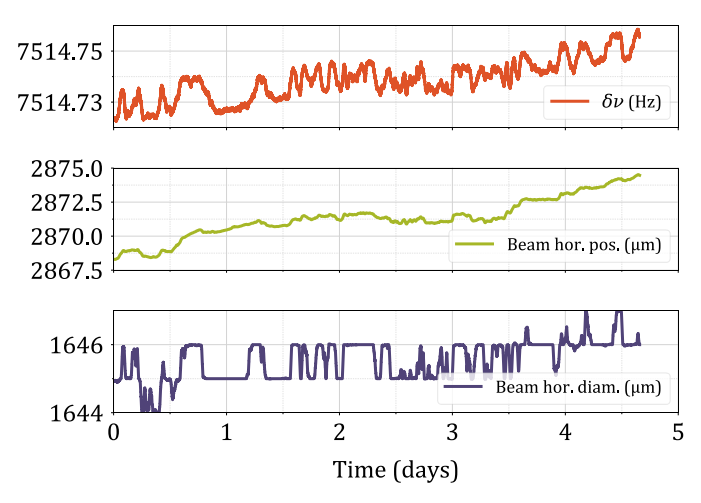


Fig. 10. Evolution of the clock frequency, the beam horizontal position and the beam horizontal diameter versus time. A moving average with a 100-pts window is applied to the datasets.

point close to the cell. In the future, we plan to distribute several sensors in the CPT package to check the impact of any possible temperature gradient along the cell. Enhanced temperature sensitivity (ETS) was observed in a POP Rb clock in [67]. In this study, temperature inhomogeneities between cell active volume and cell stem induced, through the buffer gas pressure coefficient, a relevant increase (factor of about 25) of the temperature sensitivity of the clock frequency. In Ref. [67], the ETS phenomenon was "favored" due to the use of a cell with very long stems, relative to the dimensions of the main volume of the cell, resulting in  $v_b = V_b/V = 0.08$ , with  $V_b$  the volume of the stem and V the total volume of the cell (stem + active volume). In our experiment, we estimate  $v_b \simeq 0.001$ , a value 80 times smaller than in [67]. The ETS effect should be therefore much smaller in our cell.

We also know that atoms experience a slight magnetic field gradient, of about 7 mG, along the cell length due to the insufficient length of the solenoid used to apply the magnetic field. This effect contributes to the shift and broadening of the overall 0-0 resonance by about 0.4 Hz, a value which remains small compared to the linewidth of the Ramsey-CPT fringe.

### VI. CONCLUSIONS

We have measured the dependence of the frequency of a CPT-based Cs cell atomic clock on numerous experimental parameters. The CPT clock, which combines the pushpull optical pumping (PPOP) scheme and symmetric Auto-Balanced Ramsey (SABR) interrogation, exhibits a short-term fractional frequency stability of  $2\times 10^{-13}$  at 1 s in the SABR mode, improved at  $1\times 10^{-13}$  at 1 s in the Ramsey-CPT case (with T=2.8 ms). We showed in this study that the SABR technique yields low-sensitivity coefficients of the clock frequency to the light-field parameters, including the laser power, the microwave power, and the laser frequency. It was also shown that SABR, compared with Ramsey-CPT, reduces the impact on the clock frequency of variations of the EOM bias voltage. We reported the dependence of the clock frequency on temperature variations of the EOM, the

AOM, and some passive optical components. These studies have highlighted how such temperature variations, which can affect the light-field polarization state, induce subsequent shifts of the clock frequency. The impact of mirror translation on the Michelson system has also been evaluated. To date, among the measured effects, main contributions to the clock stability at 1 day are temperature variations of the cube of the Michelson system, the laser frequency, the microwave power and the static magnetic field. Other contributions are estimated at a level lower than  $10^{-15}$  at 1 day integration time.

The clock stability budget at 1 day is to date a factor of 2.6 higher than the measured clock stability. Also, unexplained degradation of the clock stability is observed after about 100 s. The evaluation of additional contributions, including the barometric effect [65] or the enhanced temperature sensitivity (ETS) effect [67], was discussed. The observation of a correlation between the clock frequency and the geometric properties (position and diameter) of the laser beam was also reported. In future studies, we plan to investigate the impact on the clock frequency of variations of the interrogating laser beam profile. Temperature and magnetic field gradients experienced by the atoms in the CPT cell will also be evaluated.

## **A**CKNOWLEDGMENTS

The authors would like to thank the DGA (Direction Générale de l'Armement) for its financial support and fruitful discussions. The PhD thesis of J. Breurec is supported by ANRT-Cifre program. This work has been partly supported by Agence Nationale de la Recherche (ANR) in the frame of the LabeX FIRST-TF (Grant ANR 10-LABX-0048), and EquipeX Oscillator IMP (Grant ANR 11-EQPX-0033).

# REFERENCES

- B. Jaduszliwer and J. Camparo, "Past, present and future of atomic clocks for gnss," GPS Solutions, vol. 25, no. 1, p. 27, 2021.
- [2] J. Camparo, "The rubidium atomic clock and basic research," *Physics Today*, vol. 60, no. 11, pp. 33–39, 2007.
- [3] E. Batori, N. Almat, C. Affolderbach, and G. Mileti, "GNSS-grade space atomic frequency standards: Current status and ongoing developments," *Advances in Space Research*, vol. 68, no. 12, pp. 4723–4733, 2021.
- [4] T. Bandi, C. Affolderbach, C. Stefanucci, F. Merli, A. K. Skrivervik, and G. Mileti, "Compact high-performance continuous-wave double-resonance rubidium standard with 1.4 × 10<sup>-13</sup> τ<sup>-1/2</sup> stability," *IEEE Trans. Ultrason. Ferroelec. Freq. Contr.*, vol. 61, no. 11, pp. 1769–1778, 2014.
- [5] J. C. V. Formichella and P. Tavella, "Influence of the ac-stark shift on gps atomic clock timekeeping," *Appl. Phys. Lett.*, vol. 110, no. 4, p. 043506, 2017.
- [6] S. Knappe, V. Shah, P. D. D. Schwindt, L. Hollberg, J. Kitching, L.-A. Liew, and J. Moreland, "A microfabricated atomic clock," *Appl. Phys. Lett.*, vol. 85, no. 9, pp. 1460–1462, 2004.
- [7] S. Knappe, "MEMS atomic clocks," in *Comprehensive Microsystems*, Y. B. Gianchandani, O. Tabata, and H. Zappe, Eds. Oxford: Elsevier, 2008, pp. 571 – 612.
- [8] J. Kitching, "Chip-scale atomic devices," Appl. Phys. Rev., vol. 5, no. 031302, 2018.
- [9] P. Cash, W. Krzewick, P. Machado, K. R. Overstreet, M. Silveira, M. Stanczyk, D. Taylor, and X. Zhang, "Microsemi chip scale atomic clock (csac) technical status, applications, and future plans," in 2018 European Frequency and Time Forum (EFTF), 2018, pp. 65–71.
- [10] E. Arimondo, "Coherent population trapping in laser spectroscopy," ser. Progress in Optics, 1996, vol. 35, pp. 257–354.
- [11] J. Vanier, "Atomic clocks based on coherent population trapping: a review," Appl. Phys. B, vol. 81, no. 4, pp. 421–442, 2005.

- [12] J. Kitching, S. Knappe, and L. Hollberg, "Miniature vapor-cell atomic-frequency references," *Appl. Phys. Lett.*, vol. 81, no. 3, pp. 553–555, 2002.
- [13] L.-A. Liew, S. Knappe, J. Moreland, H. G. Robinson, L. Hollberg, and J. Kitching, "Microfabricated alkali atom vapor cells," *Appl. Phys. Lett.*, vol. 84, no. 14, pp. 2694–2696, 2004.
- [14] S. Knappe, V. Gerginov, P. D. D. Schwindt, V. Shah, H. G. Robinson, L. Hollberg, and J. Kitching, "Atomic vapor cells for chip-scale atomic clocks with improved long-term frequency stability," *Opt. Lett.*, vol. 30, no. 18, pp. 2351–2353, 2005.
- [15] A. Douahi, L. Nieradko, J. C. Beugnot, J. Dziuban, H. Maillote, S. Guérandel, M. Moraja, C. Gorecki, and V. Giordano, "Vapour microcell for chip scale atomic frequency standard," *Elec. Lett.*, vol. 43, no. 5, pp. 279–280, 2007.
- [16] M. Hasegawa, R. K. Chutani, C. Gorecki, R. Boudot, P. Dziuban, V. Giordano, S. Clatot, and L. Mauri, "Microfabrication of cesium vapor cells with buffer gas for MEMS atomic clocks," *Sensors Actuators A*, vol. 167, pp. 594–601, 2011.
- [17] S. Karlen, J. Gobet, T. Overstolz, J. Haesler, and S. Lecomte, "Lifetime assessment of RbN<sub>3</sub>-filled MEMS atomic vapor cells with Al<sub>2</sub>o<sub>3</sub> coating," *Opt. Express*, vol. 25, no. 3, pp. 2187–2194, 2017.
- [18] V. Maurice, J. Rutkowski, E. Kroemer, S. Bargiel, N. Passilly, R. Boudot, C. Gorecki, L. Mauri, and M. Moraja, "Microfabricated vapor cells filled with a cesium dispensing paste for miniature atomic clocks," *Appl. Phys. Lett.*, vol. 110, no. 16, p. 164103, 2017.
- [19] D. G. Bopp, V. M. Maurice, and J. E. Kitching, "Wafer-level fabrication of alkali vapor cells using in-situ atomic deposition," *Journal of Physics: Photonics*, vol. 3, no. 1, p. 015002, 2020.
- [20] V. Maurice, C. Carlé, S. Keshavarzi, R. Chutani, S. Queste, L. Gauthier-Manuel, J.-M. Cote, R. Vicarini, M. Abdel Hafiz, R. Boudot, and N. Passilly, "Wafer-level vapor cells filled with laser-actuated hermetic seals for integrated atomic devices," *Microsystems & Nanoengineering*, vol. 8, no. 1, p. 129, 2022.
- [21] D. K. Serkland, K. M. Geib, G. M. Peake, R. I. Lutwak, A. H. Rashed, M. Varghese, G. B. Tepolt, and M. D. Prouty, "Vesels for atomic sensors," in *Vertical-Cavity Surface-Emitting Lasers XI*, vol. 6484. SPIE, 2007, p. 648406.
- [22] F. Gruet, A. Al-Samaneh, E. Kroemer, L. Bimboes, D. Miletic, C. Affolderbach, D. Wahl, R. Boudot, G. Mileti, and R. Michalzik, "Metrological characterization of custom-designed 894.6 nm VCSELs for miniature atomic clocks," *Opt. Express*, vol. 21, no. 5, pp. 5781–5792, 2013.
- [23] M. Huang, D. K. Serkland, and J. Camparo, "A narrow-linewidth three-mirror VCSEL for atomic devices," Appl. Phys. Lett., vol. 121, no. 114002, 2022.
- [24] R. Lutwak, A. Rashed, M. Varghese, G. Tepolt, J. LeBlanc, M. J. Mescher, D. K. Serkland, K. M. Geib, G. M. Peake, and S. Römisch, "The Chip-Scale Atomic Clock-Prototype Evaluation," in *Proceedings of the 39th Annual Precise Time and Time Interval Meeting*, Long Beach, CA, 2007, pp. 269–290.
- [25] H. Zhang, H. Hans, N. Tharayil, A. Shirane, M. Suzuki, K. Harasaka, K. Adachi, S. Goka, S. Yanagimachi, and K. Okada, "ULPAC: A miniaturized ultra-low-power atomic clock," *IEEE Journ. Solid State Circuits*, vol. 54, no. 11, pp. 3135–3148, 2019.
- [26] R. Vicarini, M. Abdel Hafiz, V. Maurice, N. Passilly, E. Kroemer, L. Ribetto, V. Gaff, C. Gorecki, S. Galliou, and R. Boudot, "Mitigation of temperature-induced light-shift effects in miniaturized atomic clocks," *IEEE Trans. Ultrason. Ferroelec. Freq. Contr.*, vol. 66, no. 12, pp. 1962– 1967, 2019.
- [27] S. Yanagimachi, K. Harasaka, R. Suzuki, M. Suzuki, and S. Goka, "Reducing frequency drift caused by light shift in coherent population trapping-based low-power atomic clocks," *Appl. Phys. Lett.*, vol. 116, no. 104102, 2020.
- [28] C. Carlé, M. A. Hafiz, S. Keshavarzi, R. Vicarini, N. Passilly, and R. Boudot, "Pulsed-CPT Cs-Ne microcell atomic clock with frequency stability below 2×10<sup>-12</sup> at 10<sup>5</sup> s," *Opt. Express*, vol. 31, no. 5, pp. 8160–8169, 2023.
- [29] N. F. Ramsey, "A molecular beam resonance method with separated oscillating fields," *Phys. Rev.*, vol. 78, no. 6, p. 695, 1950.
- [30] S. Micalizio, C. Calosso, A. Godone, and F. Levi, "Metrological characterization of the pulsed Rb clock with optical detection," *Metrologia*, vol. 49, pp. 425–436, 2012.
- [31] N. Almat, M. Gharavipour, W. Moreno, F. Gruet, C. Affolderbach, and G. Mileti, "Long-term stability analysis toward < 10<sup>-14</sup> level for a highly compact pop rb cell atomic clock," *IEEE Trans. Ultrason. Ferroelec. Freq. Contr.*, vol. 67, no. 1, pp. 207–216, 2020.

- [32] S. Micalizio, F. Levi, C. E. Calosso, M. Gozzelino, and A. Godone, "A pulsed-laser rb atomic frequency standard for GNSS applications," GPS Solutions, vol. 25, no. 3, p. 94, 2021.
- [33] Z. Yu, Z. Du, Y. Liu, K. Wang, W. Xue, and S. Zhang, "A compact laser system for the pulsed optically pumped rubidium cell atomic clock," *IEEE Trans. Ultrason. Ferroelec. Freq. Contr.*, vol. 69, no. 3, pp. 1137– 1146, 2022.
- [34] M. Gozzelino, S. Micanizio, C. E. Calosso, J. Belfi, A. Sapia, and F. Levi, "Realization of a pulsed optically pumped rb clock with a frequency stability below 10<sup>-15</sup>," Sci. Rep., vol. 13, no. 12974, 2023.
- [35] M. A. Hafiz and R. Boudot, "A coherent population trapping cs vapor cell atomic clock based on push-pull optical pumping," *J. Appl. Phys.*, vol. 118, no. 124903, 2017.
- [36] P. Yun, F. Tricot, C. E. Calosso, S. Micalizio, B. François, R. Boudot, S. Guérandel, and E. de Clercq, "High-performance coherent population trapping clock with polarization modulation," *Phys. Rev. Appl.*, vol. 7, no. 1, p. 014018, 2017.
- [37] P. Yun, Q. Li, Q. Hao, G. Liu, E. de Clercq, S. Guérandel, X. Liu, S. Gu, Y. Gao, and S. Zhang, "High-performance coherent population trapping atomic clock with direct-modulation distributed bragg reflector laser," *Metrologia*, vol. 58, no. 4, p. 045001, 2021.
- [38] J. E. Thomas, P. R. Hemmer, S. Ezekiel, C. C. Leiby, R. H. Picard, and C. R. Willis, "Observation of Ramsey fringes using a stimulated, resonance Raman transition in a sodium atomic beam," *Phys. Rev. Lett.*, vol. 48, no. 13, pp. 867–870, 1982.
- [39] T. Zanon, S. Guerandel, E. de Clercq, D. Holleville, N. Dimarcq, and A. Clairon, "High contrast Ramsey fringes with coherent-populationtrapping pulses in a double lambda atomic system," *Phys. Rev. Lett.*, vol. 94, no. 19, p. 193002, 2005.
- [40] N. Castagna, R. Boudot, S. Guérandel, E. de Clercq, N. Dimarcq, and A. Clairon, "Investigations on continuous and pulsed interrogation for a CPT atomic clock," *IEEE Trans. Ultrason. Ferroelec. Freq. Contr.*, vol. 56, no. 2, pp. 246–253, 2009.
- [41] R. Boudot, S. Guérandel, E. de Clercq, N. Dimarcq, and A. Clairon, "Current status of a pulsed CPT Cs cell clock," *IEEE Trans. Instr. Meas.*, vol. 58, no. 4, pp. 1217–1222, 2009.
- [42] O. Kozlova, J. Danet, S. Guerandel, and E. de Clercq, "Limitations of long-term stability in a coherent population trapping Cs clock," *IEEE Trans. Instr. Meas.*, vol. 63, no. 7, pp. 1863–1870, 2014.
- [43] M. Abdel Hafiz, G. Coget, P. Yun, S. Guérandel, E. de Clercq, and R. Boudot, "A high-performance Raman-Ramsey Cs vapor cell atomic clock." J. Appl. Phys., vol. 121, no. 104903, 2017.
- [44] T. Zanon-Willette, R. Lefevre, R. Metzdorff, N. Sillitoe, S. Almonacil, M. Minissale, E. de Clercq, A. V. Taichenachev, V. I. Yudin, and E. Arimondo, "Composite laser-pulses spectroscopy for high-accuracy optical clocks: a review of recent progress and perspectives," *Rep. Prog. Phys.*, vol. 81, no. 9, p. 094401, 2018.
- [45] M. Abdel Hafiz, G. Coget, M. Petersen, C. Rocher, S. Guérandel, T. Zanon-Willette, E. de Clercq, and R. Boudot, "Toward a High-Stability Coherent Population Trapping Cs Vapor-Cell Atomic Clock Using Autobalanced Ramsey Spectroscopy," *Phys. Rev. Appl.*, vol. 9, no. 064002, 2018.
- [46] M. Abdel Hafiz, G. Coget, M. Petersen, C. E. Calosso, S. Guérandel, E. de Clercq, and R. Boudot, "Symmetric autobalanced Ramsey interrogation for high-performance coherent population- trapping vapor-cell atomic clock," *Appl. Phys. Lett.*, vol. 112, no. 244102, 2018.
- [47] Y. Y. Jau, E. Miron, A. B. Post, N. N. Kuzma, and W. Happer, "Push-pull optical pumping of pure superposition states," *Phys. Rev. Lett.*, vol. 93, no. 16, p. 160802, 2004.
- [48] X. Liu, J.-M. Mérolla, S. Guérandel, C. Gorecki, E. de Clercq, and R. Boudot, "Coherent-population-trapping resonances in buffer-gasfilled cs-vapor cells with push-pull optical pumping," *Phys. Rev. A*, vol. 87, no. 1, p. 013416, 2013.
- [49] K. G. Libbrecht and J. L. Hall, "A low-noise high-speed diode laser current controller," *Review of Scientific Instruments*, vol. 64, no. 8, pp. 2133–2135, 1993.
- [50] B. Francois, C. E. Calosso, M. A. Hafiz, S. Micalizio, and R. Boudot, "Simple-design ultra-low phase noise microwave frequency synthesizers for high-performance cs and rb vapor-cell atomic clocks," *Rev. Sci. Instr.*, vol. 86, no. 9, p. 094707, 2015.
- [51] M. A. Hafiz, G. Coget, E. Clercq, and R. Boudot, "Doppler-free spectroscopy on the cs d<sub>1</sub> line with a dual-frequency laser," *Opt. Letters*, vol. 41, pp. 2982–2985, 2016.
- [52] D. Brazhnikov, M. Petersen, G. Coget, N. Passilly, V. Maurice, C. Gorecki, and R. Boudot, "Dual-frequency sub-doppler spectroscopy: Extended theoretical model and microcell-based experiments," *Phys. Rev. A*, vol. 99, no. 6, p. 062508, 2019.

- [53] C. E. Calosso, M. Gozzelino, A. Godone, H. Lin, F. Levi, and S. Micalizio, "Intensity detection noise in pulsed vapor-cell frequency standards," *IEEE Trans. Ultrason. Ferroelec. Freq. Contr.*, vol. 67, no. 5, pp. 1074–1079, 2020.
- [54] C. E. Calosso, B. Francois, S. Micalizio, and R. Boudot, "Local oscillators and digital electronics for compact atomic clocks," Microwave Technology and Techniques Workshop (MTT'17), Noordwijk, The Netherlands, Apris 3-5, 2017.
- [55] M. Abdel Hafiz, C. Carlé, N. Passilly, J. M. Danet, C. E. Calosso, and R. Boudot, "Light-shift mitigation in a microcell-based atomic clock with symmetric auto-balanced Ramsey spectroscopy," *Appl. Phys. Lett.*, vol. 120, no. 064101, 2022.
- [56] E. Blanshan, S. M. Rochester, E. A. Donley, and J. Kitching, "Light shifts in a pulsed cold-atom coherent-population-trapping clock," *Phys. Rev. A*, vol. 91, no. 041401(R), 2015.
- [57] X. Liu, E. Ivanov, V. I. Yudin, J. Kitching, and E. A. Donley, "Low-Drift Coherent Population Trapping Clock Based on Laser-Cooled Atoms and High-Coherence Excitation Fields," *Phys. Rev. Appl.*, vol. 8, no. 054001, 2017.
- [58] J. W. Pollock, V. I. Yudin, M. Shuker, M. Yu Basalaev, A. V. Taichenachev, X. Liu, J. Kitching, and E. A. Donley, "ac Stark shifts of dark resonances probed with Ramsey spectroscopy," *Phys. Rev. A*, vol. 98, no. 053424, 2017.
- [59] M. Shuker, J. W. Pollock, R. Boudot, V. I. Yudin, A. V. Taichenachev, J. Kitching, and E. A. Donley, "Ramsey spectroscopy with displaced frequency jumps," *Phys. Rev. Lett.*, vol. 122, no. 113601, 2019.
- [60] M. Abdel Hafiz, R. Vicarini, N. Passilly, C. E. Calosso, V. Maurice, J. W. Pollock, A. V. Taichenachev, V. I. Yudin, J. Kitching, and R. Boudot, "Protocol for light-shift compensation in a continuous-wave microcell atomic clock," *Phys. Rev. Appl.*, vol. 14, no. 034015, 2020.
- [61] A. Didier, J. Millo, S. Grop, B. Dubois, E. Bigler, E. Rubiola, C. Lacroûte, and Y. Kersalé, "Ultra-low phase noise all-optical microwave generation setup based on commercial devices," *Appl. Opt.*, vol. 54, no. 12, pp. 3682–3686, 2015.
- [62] A. Gusching, J. Millo, I. Ryger, R. Vicarini, M. A. Hafiz, N. Passilly, and R. Boudot, "Cs microcell optical reference with frequency stability in the low 10<sup>-13</sup> range at 1 s," *Opt. Lett.*, vol. 48, no. 6, pp. 1526–1529, 2023
- [63] O. Kozlova, S. Guérandel, and E. de Clercq, "Temperature and pressure shift of the Cs clock transition in the presence of buffer gases: Ne, N<sub>2</sub>, Ar," *Phys. Rev. A*, vol. 83, no. 6, p. 062714, 2011.
- [64] F. Tricot, D. H. Phung, M. Lours, S. Guérandel, and E. de Clercq, "Power stabilization of a diode laser with an acousto-optic modulator," *Rev. Sci. Instr.*, vol. 89, no. 11, p. 113112, 2018.
- [65] W. Moreno, M. Pellaton, C. Affolderbach, and G. Mileti, "Barometric effect in vapor-cell atomic clocks," *IEEE Trans. Ultrason. Ferroelec. Freq. Contr.*, vol. 65, no. 8, pp. 1500–1503, 2018.
- [66] J. Pollock, V. I. Yudin, A. Taichenachev, M. Y. Basalaev, D. V. Kovalenko, A. Hansen, J. Kitching, and W. R. McGehee, "Inhomogeneous light shifts of coherent population trapping resonances," *Appl. Phys. Lett.*, vol. 120, p. 154001, 2022.
- [67] C. E. Calosso, A. Godone, F. Levi, and S. Micalizio, "Enhanced temperature sensitivity in vapor-cell frequency standards," *IEEE Trans. Ultrason. Ferroelec. Freq. Contr.*, vol. 59, no. 12, pp. 2646–2654, 2012.



J. Breurec received the master degree in mechatronics from the Engineering School IMT Mines Alès, Alès, France, in 2020. J. Breurec is currently a Ph.D. candidate at the Time-Frequency department of FEMTO-ST, Besançon, France, in collaboration with Thales, Vélizy-Villacoublay, France. Her research interests include the development of compact vaporcell atomic frequency standards.

M. Abdel Hafiz received the Ph.D. degree from Université Bourgogne-Franche-Comté, Besançon, France, in 2017. His Ph.D. thesis work, led at the Franche-Comté Electronique Mécanique Thermique et Optique-Sciences et Technologies (FEMTO-ST), Besançon, was focused on the development of a high-performance microwave Cs vapor cell atomic clock based on coherent population trapping (CPT). From March 2018 to end 2019, he has worked as a Postdoctoral Researcher with Physikalisch-Technische Bundesanstalt (PTB), Braunschweig, Germany, on the development of a transportable Yb+ ion optical clock (Opticlock). Since January 2020, he has been a Permanent Assistant Professor with the Ecole Nationale Supérieure de Mécanique et des Microtechniques (ENSMM), doing his research activities at FEMTO-ST. He is mainly involved in the development of a single Yb+ trapped-ion optical clock and vapor cell atomic clocks.



C. E. Calosso was born in Asti (Italy) in 1973. In 2002, he received his Ph.D. degree in communication and electronic engineering at the Polytechnic of Turin (Italy) and, in the same year, he joined to IEN. Now he is permanent researcher at INRIM (Italy), where he develops low noise digital electronics for time and frequency applications. His activities include primary frequency standards, vapor cells clocks, frequency dissemination over fiber links, phasemeters, frequency division and synthesis and, recently, real-time

time scale generation. He is also interested in signal analysis, with particular attention to the role of aliasing in time interval counters and two-sample variances.

Oriane Lelièvre Biography and photograph not available.



R. Boudot received his Ph.D. degree in engineering sciences, in 2006, from Université de Franche-Comté, Besancon, France. From 2007 to 2009, R. Boudot was a post-doctoral researcher at the Systèmes de Références Temps-Espace laboratory (SYRTE, Paris, France). Since October 2008, R. Boudot has been a permanent CNRS researcher at FEMTO-ST. His research interests include compact and miniature cell atomic clocks, low noise electronics, oscillators, frequency synthesizers

and laser spectroscopy. Since January 2017, R. Boudot has been the Head of the OHMS Group at Time-Frequency department of FEMTO-ST. From April 2018 to July 2019, R. Boudot has worked as a NIST Guest Researcher, in Atomic Devices and Instrumentation (ADI) Group, on laser cooling experiments in microfabricated cells, cold-atom clocks and sensors. R. Boudot has awarded the EFTF Young Scientist Award in 2020.